PHYSICS OF FLUIDS **25**, 043304 (2013)

Turbulent flow characteristics in a randomly packed porous bed based on particle image velocimetry measurements

Vishal A. Patil and James A. Liburdy
School of Mechanical, Industrial and Manufacturing Engineering, Oregon State University, Corvallis, Oregon 97331, USA

(Received 13 December 2012; accepted 18 March 2013; published online 23 April 2013)

An experimental study was undertaken to better understand the turbulent flow characteristics within a randomly packed porous bed. A relatively low aspect ratio bed (bed width to spherical solid phase particle diameter of 4.67) with the fluid phase refractive index matched to that of the solid phase was used to obtain time resolved particle image velocimetry data. Care was taken to assure that data were outside of the wall affected region, and results are based on detailed time dependent velocity vector maps obtained at selected pores. In particular, four pores were identified that display a range of very disparate mean flow conditions which resemble channel-like flow, impinging flow, recirculating flow, and jet like flow. Velocity data were used for a range of pore Reynolds numbers, Re_{pore}, from 418 to 3964 to determine the following turbulence measures: (i) turbulent kinetic energy components, (ii) turbulent shear production rate, (iii) integral Eulerian length and time scales, and (iv) energy spectra. The pore Reynolds number is based on the porous bed hydraulic diameter, $D_H = \phi D_B/(1-\phi)$ where ϕ is bed porosity and D_B is solid phase bead diameter and average bed interstitial velocity, $V_{int} = V_{Darcy}/\phi$, where $V_{Darcy} = Q/A_{bed}$, with Q being the volumetric flow rate and A_{bed} the bed cross section normal to the flow. Results show that when scaled with the bed hydraulic diameter, D_H, and average interstitial velocity, V_{int}, these turbulence measures all collapse for Re_{pore}, beyond approximately 2800, except that the integral scales collapse at a lower value near 1300–1800. These results show that the pore turbulence characteristics are remarkably similar from pore to pore and that scaling based on bed averaged variables like D_H and V_{int} characterizes their magnitudes despite very different mean flow conditions. © *2013 AIP Publishing LLC*. [http://dx.doi.org/10.1063/1.4802043]

I. INTRODUCTION

Turbulent flow is encountered in many natural and man-made porous systems. A good review for an introduction and applications of these flows can be found in the book by De Lemos.[1] One application where turbulence in a porous structure is observed is in the operation of fixed bed reactors which are routinely used in the synthesis of basic chemicals and intermediates on large scales using gaseous reactants. Random packing of porous spheres (such as catalyst pellets) is one of several geometric arrangements used in practice for constructing fixed bed reactors. These reactors are configured in both low and high aspect ratio beds in industrial and/or laboratory environment. Here, the aspect ratio is defined as the bed span, or width, W, divided by the solid phase characteristic length. For spherical beads with diameter D_B, the aspect ratio is W/D_B. Even though transport processes and dispersion properties are important information necessary in development, design, and control of a catalytic reactor, experimental investigation of pore scale turbulent flow physics is absent. The occurrence of turbulence in flow in a porous structure was reported by Dybbs and Edwards[2] utilizing a simple dye visualization of flow through a bed formed by rods in regular, hexagonal packing. It is necessary to rely on established correlations for predicting transport and dispersive properties of flow in fixed beds and ultimately in reactor design (Andrigo *et al.*,[3] Eigenberger[4]). Global bed parameters like pressure drop, axial dispersion, and longitudinal dispersion have been measured and

correlations have been developed for this purpose (Dixon and Cresswell,[5] Ergun,[6] Gunn,[7] Wen and Fan[8]).

Some effort has been made towards the development of models to take into account transport properties of these flows. The development of Reynolds averaged Navier-Stokes (RANS) equations for modeling flow at the pore scale has been attempted by numerous researchers and is reviewed in de Lemos and Pedras.[9] These RANS equations have been derived by time averaging the volume-averaged extended Darcy-Forchheimer model equations (Antohe and Lage,[10] Getachew *et al.*[11]), or by volume averaging the time-averaged Reynolds-averaged equations (Masuoka and Takatsu,[12] Nakayama and Kuwahara[13]), or by a double-decomposition technique based on exchangeability of volume-time or time-volume averaging (Pedras and de Lemos[14]). In this latter approach extra source terms, arising due to the existence of the solid phase in the bed, are closed by conducting numerical experiments on simple geometries such as periodic array of square or cylindrical rods. In general, these models lack validation with experimental or Direct Numerical Simulation (DNS) results and hence are limited in general applicability.

The transport processes and turbulent dispersion within a bed is expected to be functionally dependent on the overall packing geometry and tortuosity associated with the bed. In general, within a pore (which may be formed, say, among catalyst pellets in a reactor bed) the dispersive characteristics would be dominated by the fluid phase convective motion within the pore. However, this pore level flow, in general, is expected to be greatly influenced by the flow connectivity with surrounding pores. Detailed studies of pore level flow dynamics would provide insight and may lead to improved models to account for non-homogeneous distribution of temperature and concentrations which are typically assumed to be uniform in many existing models (Andrigo *et al.*,[3] Eigenberger[4]). Experimentally, the pore level flows can by studied by application of particle displacement measurement techniques like particle image velocimetry (PIV) and particle tracking velocimetry (PTV) in a refractive-index matched porous bed. PIV and PTV techniques have been employed to study steady flow fields in porous beds, (Northrup *et al.*,[15] Saleh *et al.*,[16] Huang *et al.*,[17] Lachhab *et al.*,[18] Moroni and Cushman,[19] Peurrung *et al.*,[20] Stephenson and Stewart,[21] Patil and Liburdy[22]). However, obtaining reliable data is difficult because of inherent sensitivity to refractive index mismatch between the solid and liquid phases (Patil and Liburdy[23]). Nevertheless, carefully designed experiments can lead to high resolution time resolved PIV data to better understand the pore scale flow physics, useful in developing realistic models and providing measurements for validation of numerical simulations.

The goal of this paper is to quantitatively explore and identify the characteristics of the turbulent flow in a randomly packed porous bed of spherical beads. The results extend from the inertial region up into the developed turbulent regime (which is identified herein for the various turbulence quantities based on scaled asymptotic values). Several typical pore geometries are identified and their distinguishing flow characteristics are described. Statistical turbulence quantities are measured including turbulent kinetic energy spectra, turbulent kinetic energy production rates, integral Eulerian length and time scales, as well as the mean velocity variance within pores. Results are scaled with bed averaged variables such as average interstitial velocity, V_{int} and hydraulic diameter, D_H, and are used to show how results reach asymptotic values at sufficiently high Reynolds numbers.

II. EXPERIMENTAL SETUP

The experimental setup used for time resolved PIV measurements in this study is shown in Fig. 1, which illustrates the flow loop and a more detailed illustration of the flow geometry through the test section. The flow loop uses a large reservoir tank at atmospheric conditions, with a Moyno® pump used to establish the flow rate through the system. A flowmeter (Kobold, Model: MIK) was used to measure the volumetric flow rate, Q. A pressure transducer (Omega Engineering, Inc., Model: PX212-200AV) was also used but just to monitor the test loop pressure to assure there were no problems with over pressurizing the test section. After exiting the test section, the flow was pumped back into the reservoir tank forming a continuous loop.

The test section was fabricated using a square cross section duct (W × W: 70 mm × 70 mm inside dimensions) with transparent walls made from Pyrex®. The duct was 90 mm long and was filled with 15 mm diameter, D_B, optical grade beads of Pyrex. An inlet plenum was used to slow the

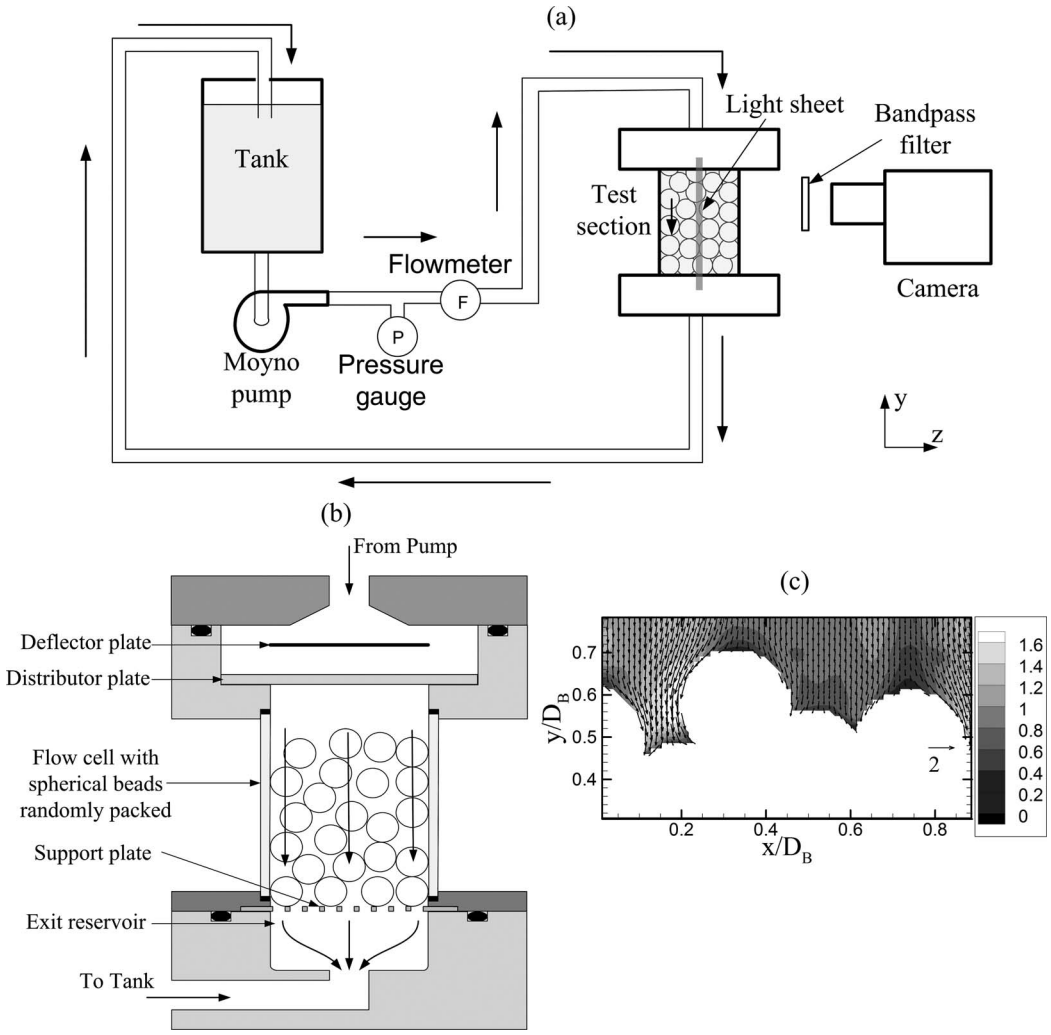

FIG. 1. Schematic of the experimental test setup used to record images, (a) flow loop, (b) detailed test section, (c) bed entrance normalized velocity field plot overlaid with contour plot of normalized velocity magnitude for $Re_{pore} = 3964$, velocity field is scaled with average interstitial velocity, V_{int}.

velocity and assure a uniform flow and pressure at the top inlet of the bed. A distributor plate was placed $0.75D_B$ upstream of the beads which had 1 mm diameter holes in a honeycomb pattern with a center spacing of 2 mm to further assure a relatively uniform inlet flow condition. The velocity was measured $0.67D_B$ downstream of the distributor plate when there were no beads in the test section and the velocity profile was uniform to within 10% of the mean value except very close to the walls. The entrance region flow above the beads is shown in Fig. 1 as both a vector plot and normalized velocity magnitude contours, based on the average interstitial velocity V_{in}.

The bed was filled in a random manner and the test section shaken to provide as close a packing as possible. The same bead configuration was used for all data sets. The bed porosity, ϕ, was measured by direct volume measurements to be 0.454, with an aspect ratio (width to bead diameter ratio) of $W/D_B = 4.67$. This is a relatively low aspect ratio bed, which implies that the walls are influencing the value of the bed porosity (larger porosity in the wall regions). A study was undertaken to better understand the random bed packing characteristics. Details of the procedure are provided by Patil and Liburdy,[22] which are briefly described as follows. Images of six planar vertical slices were obtained across the bed from locations of $0.8D_B$–$2.3D_B$ as measured from the test section walls. The image data of the solid phase were used to determine the bead locations

within the bed accounting for variations of magnification. With this information a geometric spatial autocorrelation function was determined within each plane, using zero for the solid phase and one for the fluid phase. This function was used to evaluate the packing characteristics within the bed. Near the walls the correlation function is shown to have a cyclic pattern with a period of approximately $1.0D_B$ indicating an ordered packing. In contrast, the autocorrelation near the bed center decays monotonically to a value very close to the porosity of the bed, with no cyclic behavior. This indicates that the cyclic pattern of the bead packing observed in the near wall is eliminated near the bed center and that the packing is essentially random. All velocity data presented here are located near the bed center.

An aqueous solution of ammonium thiocyanate (NH_4SCN) was the liquid phase used in this study, which has a viscosity, ν, of 1.44 cP and density, ρ, of 1.118 g/ml. The fluid phase index of refraction was varied by adjusting the solution concentration, and was matched to that of the Pyrex spheres and bed walls. This was necessary to make porous bed transmissive and nondistorting to the light sheet and imaging optics. The liquid refractive index was measured using a refractometer (Atago Co., Model: R5000, with resolution of ± 0.0005) evaluated at the sodium D line, 589.3 nm. All data were obtained with the index matching to within ± 0.0005. Complete details of the evaluation of the errors associated with a mismatch of index of refraction in a porous bed for PIV measurements is given in Patil and Liburdy.[23]

The imaging system was based on pulsed lighting from a Nd-YLF laser at a wavelength of 527 nm (New Wave Research, Pegasus PIV) and a CMOS camera (Integrated Design Tools, Inc., Model: MotionPro™ X-3) fitted with an adjustable focusing lens (Nikon AF Micro-NIKKOR 60 mm *f*/2.8D). All data were collected using an *f*-number setting of 4 and magnification ranging from 0.82 to 0.99. Depending on the value of Re_{pore}, the sampling frequency for each vector field ranged from 80 to 400 Hz, from lowest to highest Re_{pore}. The seed particles were nominally 10.7 $\pm$ 3.5 μm diameter silver coated glass microspheres. The subregion interrogation window was 32 $\times$ 32 pixels, using 50% overlap, resulting in a velocity vector spacing ranging from 66 to 80 vectors per bead diameter, depending on the magnification, or approximately 0.2 mm. Seed particle position displacements were determined using the multi-grid, multi-pass adaptive correlation method with a central differencing based window offset method. A high accuracy subpixel peak fitting algorithm specific to Dantec® software was also used. A moving average validation scheme was used to reject outliers, with a vector rejection rate of less than 1%.

In this paper, results are presented for pore Reynolds numbers ranging from $Re_{pore} = 418$ to 3964. This Reynolds number is based on the porous bed hydraulic diameter, $D_H = \phi D_B/(1-\phi)$ and average pore, or interstitial, velocity, $V_{int} = V_{Darcy}/\phi$, were $V_{Darcy} = Q/A_{bed}$, with Q being the volumetric flow rate and A_{bed} the bed cross section normal to the flow. Measures of the turbulence characteristics are presented which include turbulent kinetic energy components as well as its shear production rate, integral Eulerian length and time scales, and the mean velocity variance within pores (important for dispersion estimates). Results are scaled with the bed averaged variables, D_H and V_{int}, and shown as a function of Re_{pore}.

III. UNCERTAINTY ANALYSIS

The uncertainties of the velocities were analyzed for the various contributions to the PIV data. Error analysis was performed on instantaneous PIV data collected for pore Reynolds number, Re_{pore}, of 3964. Table I includes five error sources: magnification, refractive index mismatch, in-plane loss of image pairs (or bias error), finite number of image pair (or random error), and finally error due to perspective motion. Each are quantified and related to the measured maximum pixel displacement in the two coordinate directions. The total errors were determined and are given in both pixel count and percent of maximum displacement. The results of the total error are 1.19% in the cross stream or transverse direction and 1.0% in the downstream or longitudinal direction. Details of the determination of errors due to refractive index mismatch can be found in Patil and Liburdy[23] and the magnification error and methodology used to find the other errors is given in Patil and Liburdy.[22] Briefly, for estimating bias error due to in-plane signal loss and random error due to finite number of seed images in the interrogation window, an image shifting procedure was employed. Image shifting

TABLE I. Uncertainty estimates.

Error source	Δx	Δy
Max displacement (pixels)	7.9	9.9
Magnification, σ_{mag} (pixels)	0.024	0.03
Refractive index mismatch error, σ_{R} (pixels)	0.044	0.044
In-plane loss of image pairs (bias), σ_{bias} (pixels)	0.016	0.016
Finite number of image pairs (random), σ_{rms} (pixels)	0.025	0.025
Out-of-plane motion (perspective), σ_{p} (pixels)	0.074	0.079
Total error, σ_{T} (pixels)	0.094	0.1
Total error (% of max)	1.19	1.0

in subpixel units was accomplished by using a bicubic interpolation scheme implemented in ImageJ software. The perspective error was determined using an estimate for out-of-plane seed displacement over the entire field to be equal to the measured average x (or transverse) displacement which for the analyzed instantaneous vector map was 1.8 pixels.

Estimation of velocity gradient was accomplished using central difference scheme. Assuming nearby vectors to have nearly equal bias errors, error in velocity gradient is mostly affected by random error in velocity measurement. The random error in velocity gradient due to propagation of random error in velocity measurements was estimated to be 4.42 s^{-1} (1.5% of max) for highest Re_{pore} case of 3964.

The number of instantaneous time maps collected for each Re_{pore} at each location was 1600. Approximately 230 of these maps can be considered statistically independent as temporal autocorrelation function decays to zero past $7\Delta t$, where Δt is separation time between vector maps. Therefore, random error in time averaged mean velocity field estimation is expected to reduce by order (10^{-1}) due to large number of independent realizations of instantaneous velocity field. For similar reasons, pore averaging operator is expected to reduce the random error further by order (10^{-2}).

IV. RESULTS

Results are presented of the time resolved PIV measurements of the two components of velocity within a plane spanning the porous bed. The time resolved data sets were used to obtain statistical quantities within individual pores. Various pores were scanned using preliminary results to help identify initial characteristics that differ from pore to pore. After identifying four different pore geometries with differing flow structures, the PIV system was zoomed in for each pore independently. Figure 2 illustrates the instantaneous velocity fields for these four pores at a Reynolds number of $Re_{pore} = 3964$. All of these pores are located near the bed center, more than one and a half bead diameters from any wall as well as the entrance and exit to the test bed. Each pore has been identified based on the general mean flow structure observed within the pore. Figure 2(a) represents a channel-like flow where mean flows into the pore merges and exits the pore along multiple paths; Fig. 2(b) represents an impinging channel flow where a high velocity mean flow impinges onto a solid bead resulting in a transient stagnation region; Fig. 2(c) is a flow with a large recirculation region which is a result of flow behind a spherical bead; and Fig. 2(d) is a jet-like flow with high velocity flow entering the pore region through a small gap resulting in significant shear. These descriptions are based on a number of observations within the various pores and are used to identify different mean flow patterns and conditions which are expected to influence the nature of the turbulence within the pore. To better observe the mean flow structure in these identified "typical pore" flow regions shown in Fig. 2, the mean velocity magnitudes were normalized using V_{int}, and contours are shown in Fig. 3 for $Re_{pore} = 2860$ along with the velocity vector plots which indicate direction only. The flow structures identified above can be observed. The nature of the turbulence in these regions characterized using statistical and velocity field decomposition techniques are discussed in Secs. IV A–IV D.

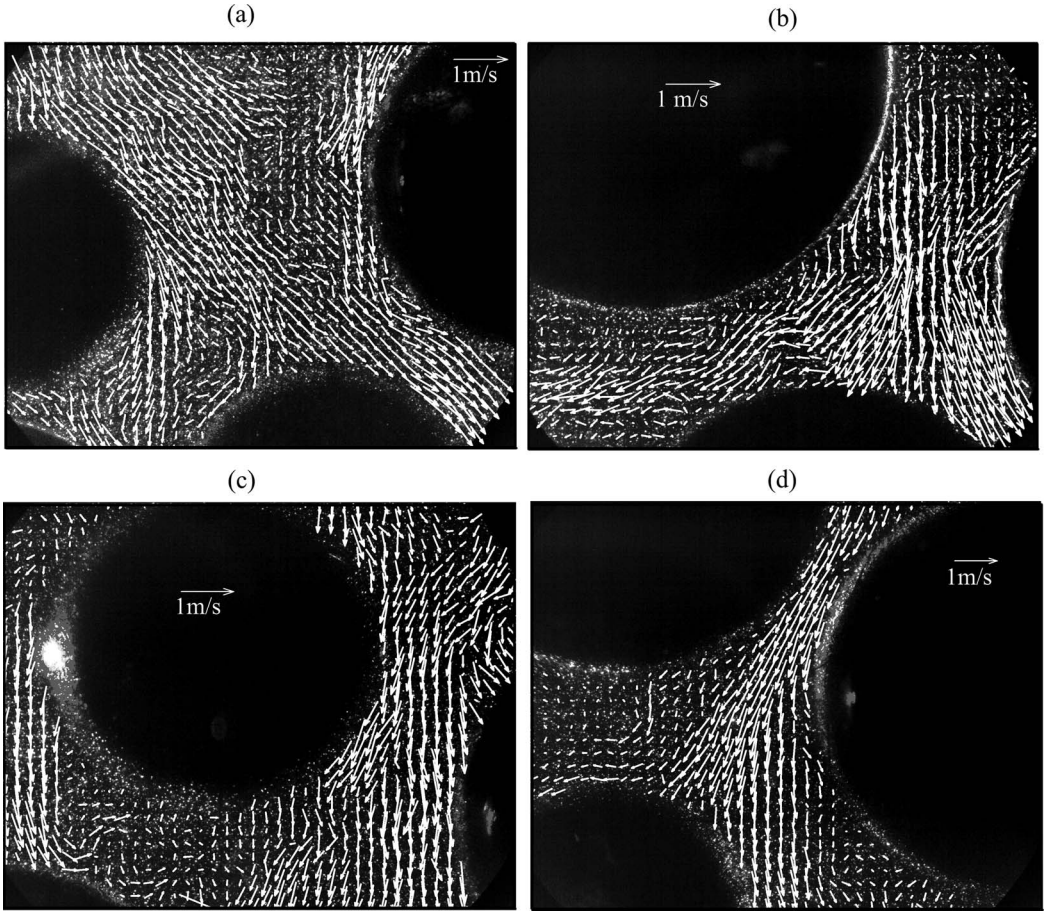

FIG. 2. Instantaneous velocity maps overlaid over raw camera image in 4 different pores in bed obtained at $Re_{pore} = 3964$; the pores are described in the paper and identified as the following: (a) channel-like region, (b) impinging region, (c) recirculation region, and (d) jet-like region.

Instantaneous velocity maps were collected for steady flow with Re_{pore} of 54 at the same locations discussed in Fig. 2 and showed no vortices, either stationary or convected, in the pore spaces. At Re_{pore} of 418, large flow structures such as recirculation regions and jet-like regions were seen at all locations. These structures were found to be highly unsteady with no dominant peak found in the temporal frequency domain. The unsteady nature of the large flow structure is illustrated in Fig. 4 for the channel like flow pore, shown in Fig. 2(a), for a value of Re_{pore} of 418. For this pore, flow mainly enters from the upper left and forms a relatively high velocity region which clearly sways back and forth at an estimated frequency near 1 Hz for this value of Re_{pore}. Similar pore scale flow oscillations occur for each pore at this value of Re_{pore}.

As Re_{pore} is increased, the large pore scale structures tend to be less dominant in favor of smaller scale vortical flow structures occurring throughout the pore space. To better observe this Large Eddy Scale (LES), filtering was applied to the instantaneous flow field. The instantaneous velocity field was filtered with a top hat filter over a range of filter sizes; the one shown in Fig. 5 has a filter size of $0.2D_B$. The filtered vector field represents the larger scale events and was then subtracted from the instantaneous vector field to yield the smaller scale flow structure. See Adrian *et al.*[24] for details on the procedure. At the lowest value of Re_{pore} shown, 418, the use of LES filtering does not indicate any visible occurrence of convected swirling flow structures which has been shown to exist in turbulent flow. This flow is unsteady, yet not believed to be turbulent, and the filtered small scale flow is rather random in nature. At the higher Re_{pore} value of 839, the swirling, vortical flow structures are very evident. The well-defined swirling flow elements are well distributed throughout

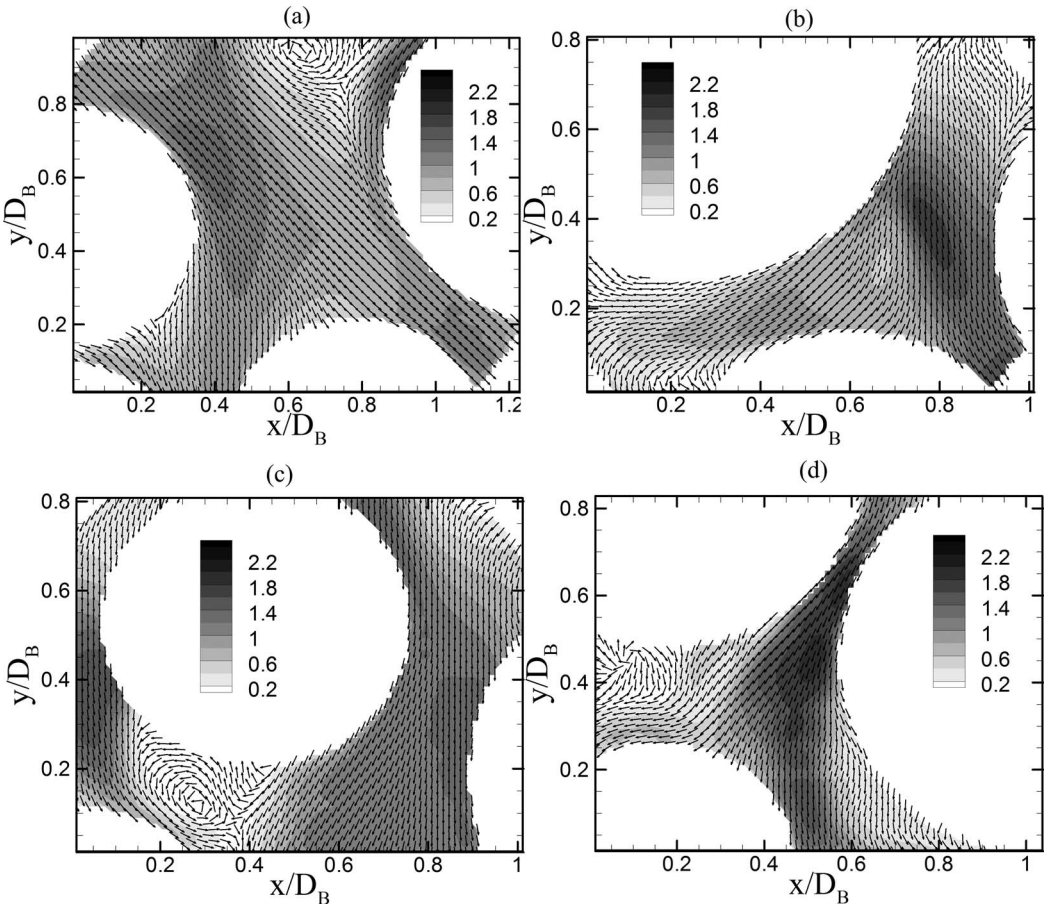

FIG. 3. (a)–(d) Mean velocity magnitude contours normalized with V_{int}, overlaid with the vector plot indicating direction only for $Re_{pore} = 2860$ for pore locations discussed in Fig. 2.

the pore space. As the value of Re_{pore} is increased up to 3964, the instantaneous map of swirling vortical flow elements observed through the LES analysis are not observed to change significantly, as seen in Figs. 5(c) and 5(d).

A. Scales of turbulence

To better understand the pore level scaling, the spatial autocorrelation was determined for each pore over the full range of Re_{pore} and are shown in Fig. 6 for the pore in Fig. 2(a) using the longitudinal fluctuating velocity component, v. The autocorrelation function in the longitudinal direction is defined below in terms of a longitudinal separation distance s

$$\langle \rho_L(s) \rangle^f = \frac{\overline{v(x, y, t)v(x, y + s, t)}}{\overline{v(x, y, t)v(x, y, t)}}, \tag{1}$$

where $\langle \rho_L \rangle^f$ is the pore averaged value of the autocorrelation function and the operator $\langle \cdot \rangle^f$ indicates pore averaged value. Results are shown in Fig. 6 where s is normalized by the hydraulic diameter, D_H. At the lowest value of Re_{pore}, the autocorrelation function remains near one up until $s/D_H \sim 0.1$, then drops rapidly with increasing s. The noted unsteady flow associated with $Re_{pore} = 418$ has of a very large scale spanning a large portion of the entire pore, as indicated in Fig. 4, with essentially no apparent smaller scale flow structures, as shown in Fig. 5. Whereas for larger Re_{pore} values, the autocorrelation function drops quickly, which indicates a loss of relatively large scale coherence.

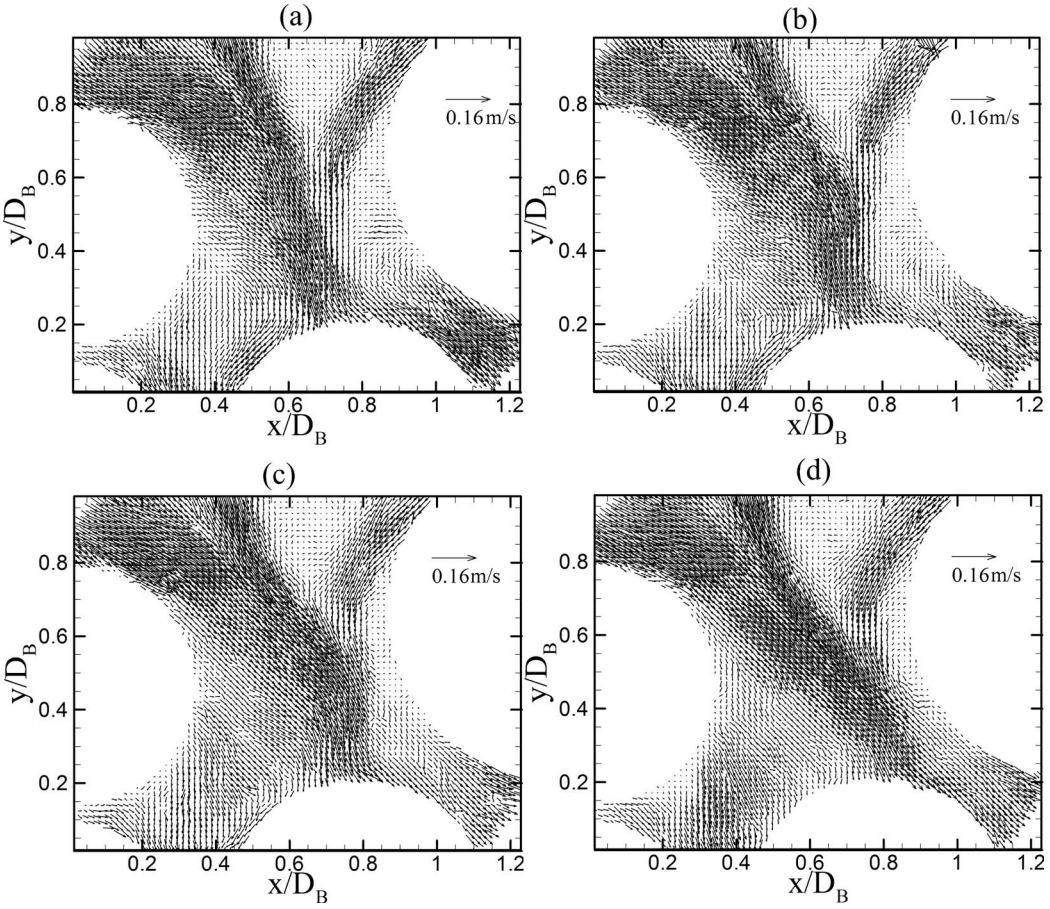

FIG. 4. (a)–(d) Sequence of instantaneous vector field at time interval of 37.5 ms (approximately 75% of integral time) for $Re_{pore} = 418$ for pore location discussed in Fig. 2(a).

As Re_{pore} increases beyond approximately 1800, all results are seen to collapse to a single curve indicating that the hydraulic diameter scales the correlation function well.

The correlation results for the larger Re_{pore} values decrease towards zero at approximately $s/D_H = 0.4$. Integration of the correlation functions with respect to s/D_H up to the first zero crossing was used to determine the pore averaged longitudinal integral length scale, $\langle L_L \rangle^f$, for each pore versus Re_{pore}. The results are shown in Fig. 7 normalized by D_H, where $L_{L,avg}$ represents an area weighted average value of all pores studied. Depending on which pore is evaluated the value of the integral length scale for low Re_{pore} varies over a range of an order of magnitude (0.025 to over 0.25). Beyond Re_{pore} of approximately 1800, indicated as the dashed line in the figure, the ratio of length scale to hydraulic diameter when averaged over the various pores reaches a fairly constant value for all four pores of $\langle L_L \rangle^f / D_H = 0.1$ with a range of values of 0.9–0.11 for the different pores. These results suggest that for the different mean flow characteristics and pore geometries, the integral length scale can be characterized by the hydraulic diameter for the porous bed. Here, the integral length scale is approximately an order of magnitude smaller than the hydraulic diameter. In turbulent flows which exhibit nearly isotropic conditions, a mixing, or integral, scale has been defined as $l = 2\,L_L$ (Tennekes and Lumley[25]). Using this estimate, it is found that the isotropic mixing length scale for the porous bed becomes: $l_{pore} \sim D_H/5$, or since $D_B = 0.83 D_H$, $l_{pore} \sim D_B/6$.

The temporal autocorrelation function was also determined for the longitudinal fluctuating velocity for each point in the pores. This was then used to determine the spatial distribution of the local Eulerian integral time scale, T_E. The value of T_E was determined by integrating the temporal autocorrelation function up to its first zero crossing. From this the pore averaged Eulerian integral

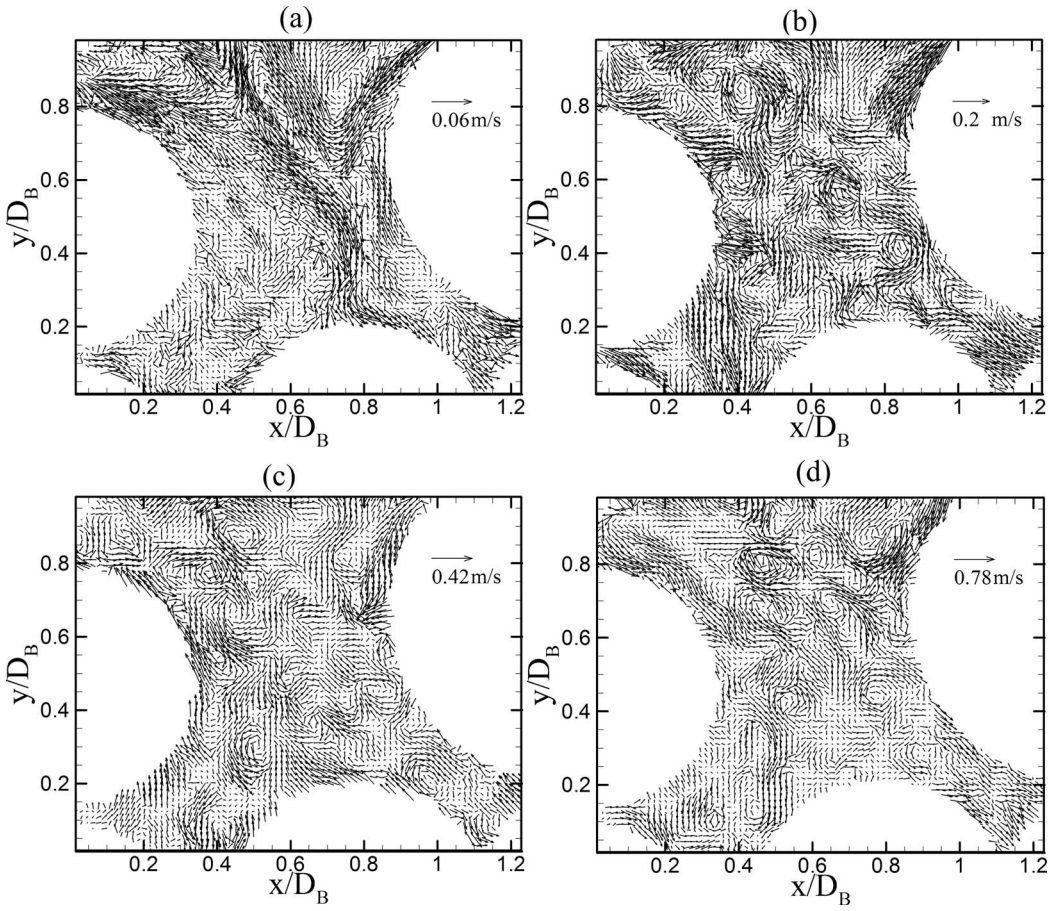

FIG. 5. Small scale component of Large Eddy Scale (LES) filtered velocity vector plots for pore space shown in Fig. 2(a) for four values of Re_{pore}: (a) 418, (b) 839, (c) 2860, and (d) 3964.

time scale, $\langle T_E \rangle^f$ was calculated by averaging values within fluid phase of the pores discussed in Fig. 2. The results are plotted in Fig. 8 versus Re_{pore} for each of the four pores. The results for each of the pores is similar in that they reach a nearly constant value beyond Re_{pore} of approximately 1300. The area weighted average for all four pores, $T_{E,avg}$, is also shown which is estimated to reach a value near $0.18D_H/V_{int}$. This shows that an integral time, when scaled with the convective time scale through the pore, is on the order of 1/5, which is very nearly the same as the integral length scale based on the hydraulic diameter of the bed.

It should be noted that the temporal autocorrelations are based on only seven data points per case at the highest Re_{pore} due to the available time resolution. However, the spatial autocorrelations are based on over 20 points per case. In order to arrive at a more exact asymptotic limit for integral time scale, T_E, would require greater time resolution. Despite this limitation, the asymptotic limit near $Re_{pore} = 1800$ found for the normalized integral length scale seems to coincide well with the value of the asymptotic turbulent regime found experimentally for the normalized pressure drop in packed beds given by Burke and Plummer,[26] see Fig. 8 in the study by Ergun.[6]

The Fourier transform of the spatial autocorrelation function was used to determine the pore averaged spatial energy spectra of the fluctuating velocity, denoted as $\langle E(\kappa) \rangle^f$. The spatial Fourier transform was carried out on the time averaged spatial autocorrelation function determined for the lateral fluctuating velocity component for each of the pores. The spectra were scaled with the pore average lateral fluctuating velocity variance, $\langle u'^2 \rangle^f$ and D_H, while the wave number, κ, was scaled with D_H. Figure 9(a) shows the spectra for several values of Re_{pore} for the pore shown in Fig. 2(a). Also shown in the figure is a dashed line indicating a $-5/3$ power law which has been modified by

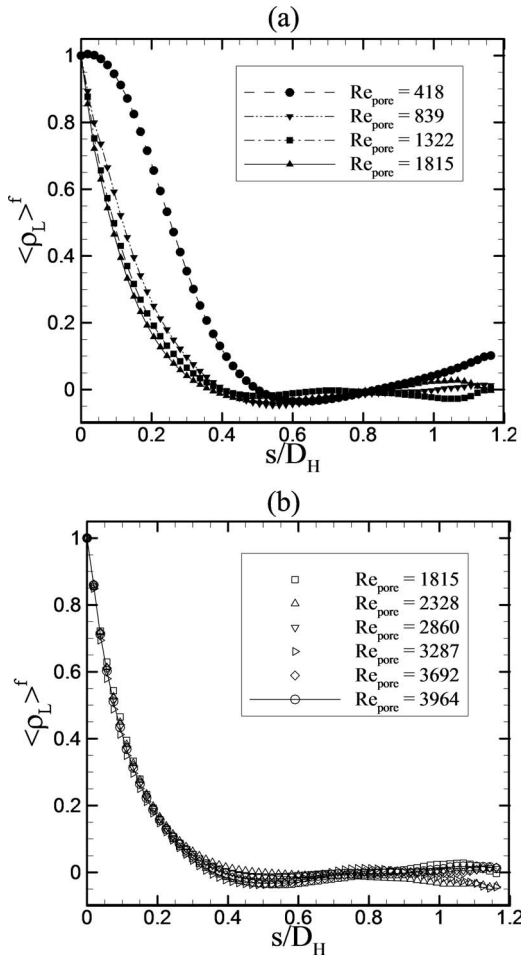

FIG. 6. Longitudinal spatial autocorrelation function, $\langle \rho_L \rangle^f$, collected in pore space shown in Fig. 2(a) (a) $Re_{pore} = 418$–1815 and (b) $Re_{pore} = 1815$–3964.

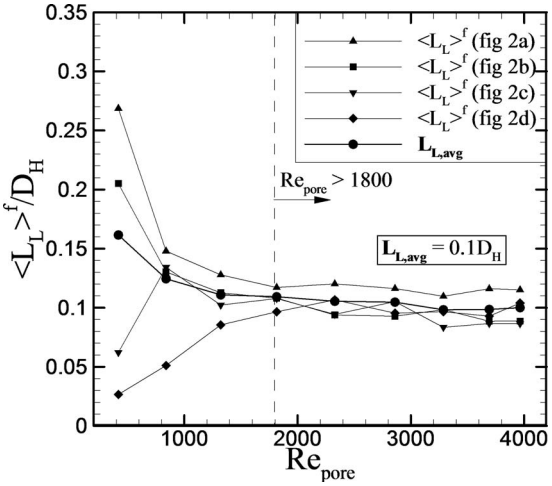

FIG. 7. Normalized Eulerian integral longitudinal length scale, $\langle L_L \rangle^f / D_H$, evaluated for data collected in pore space shown in Fig. 2.

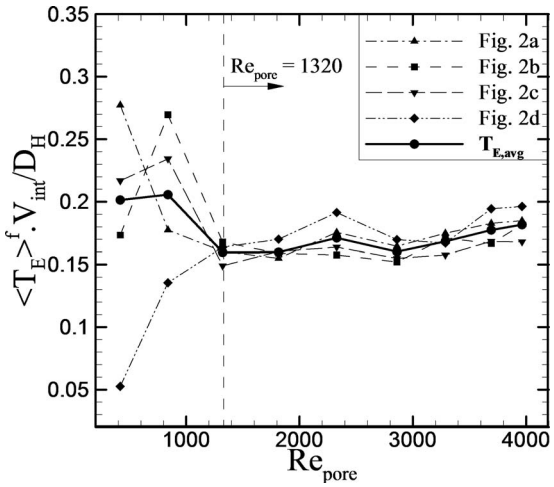

FIG. 8. Normalized Eulerian integral time scale, $\langle T_E \rangle^f V_{int}/D_H$, versus Re_{pore} evaluated for each pore shown in Fig. 2.

adding the asymptotic noise level found experimentally over the entire range of the spectrum. The added noise is the asymptotic limit at high values of κ shown in the figure. Adding the noise level results in a nonlinear trend for the $-5/3$ line on the log-log plot. Note also that this $-5/3$ line has been shifted up an arbitrary amount to make it visible on the plot. For increasing Re_{pore}, the spectra tend to follow the same trend and show a collapse to a single scaled spectrum based on the scaling selected. This trend is consistent with the smaller scale LES filtered data shown in Fig. 5 where distinct turbulent like vortical structures are shown at $Re_{pore} = 839$. The spectra for all four pores for $Re_{pore} = 3964$ are given in Fig. 9(b). Each pore tends to follow the same trend, with the only difference being the pore shown in Fig. 2(d), which has slightly elevated energy at the smaller scales and lower energy at the larger scales. This flatter profile occurs for the pore geometry that has a flow with a high shear rate, or jet-like flow. The higher energy associated with the high shear regions may be resulting in somewhat higher energy at the smaller scales.

The rms velocity fluctuations within the measurement plane were determined based on the time series data at each measurement location. Representative contour plots of the normalized longitudinal fluctuating velocity variance, $v'^2/V_{int}{}^2$, are given in Fig. 10 for four values of Re_{pore} for the pore space shown in Fig. 2(a). Note that the scale used is the same for all plots. As Re_{pore} increases, the spatial variation becomes much more uniform within the pore, with the exception of the pore in Fig. 2(d). Those areas that are more disparate are those associated with low variance regions associated with recirculation regions, such as in the upper right part of the pore in Fig. 2(a) (there is a bead just above this region just out of view) and below the bead in Fig. 2(c). Higher variance regions occur in the jet-like flow in Fig. 2(d). It should be noted that beyond approximately $Re_{pore} = 2860$, the normalized contour maps are very similar. To help illustrate the Re_{pore} variation, histograms of the normalized variance are given in Fig. 11 for the flow in Fig. 2(a). At the lower Re_{pore} values, the variance values at the peaks vary significantly from approximately 0.02 to 0.20 with rather broad distributions. The peaks tend to shift from low variance values at lower Re_{pore} values to the highest value near $Re_{pore} = 1322$, and then there is a decrease as Re_{pore} reaches approximately 2860. For Re_{pore} beyond 2860, the histograms, shown in Fig. 11(b), are nearly identical with peak variance values near 0.1, representing approximately 30% of the total count. This latter condition of nearly 1/3 of all values at approximately 0.1 is indicative of the relatively uniform contour maps shown in Fig. 10 for the high Re_{pore} conditions.

The longitudinal fluctuating velocity variance distributions within pores were determined for all of the four pores shown in Fig. 2. The pore average value, normalized by the interstitial velocity, $\langle v'^2 \rangle^f / V_{int}{}^2$, was determined for each Re_{pore} value and is plotted in Fig. 12. The value at low Re_{pore} is consistent for each pore, indicative of the onset of unsteady inertia dominated flow. Each pore demonstrates a rise of variance with increasing Re_{pore} and a subsequent decrease to a point where

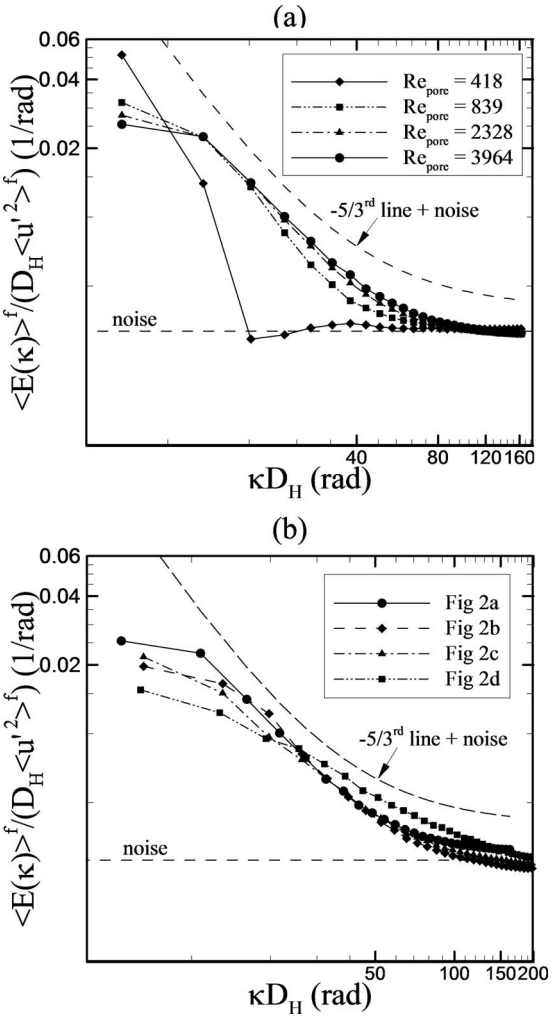

FIG. 9. Turbulent kinetic energy spectrum for (a) $Re_{pore} = 839, 2328, 3964$ and (b) $Re_{pore} = 3964$ for each pore shown in Fig. 2; the $-5/3$ line represents a slope of $-5/3$ in a log-log plot with the asymptotic noise level at high values of κ added across the spectrum, note that this line is shifted up for clarity.

the normalized variance becomes essentially independent of Re_{pore}. This Re_{pore} value at which this asymptotic limit is reached is difficult to identify, but these data indicate that at 2860 the normalized variance seems to have reached a constant value, with a pore area weighted average value for all pores, ${v'^2}_{avg}$, of approximately 0.11 ${V_{int}}^2$, with a range of 0.10–0.14. Similar results were obtained for the pore average of the lateral velocity component variance, $\langle {u'}^2 \rangle^f / {V_{int}}^2$, as shown in Fig. 13. A similar trend is noted for three of the four pores. The area weighted average value of all pores, ${u'^2}_{avg}$, is approximately 0.09 ${V_{int}}^2$ with a range of 0.05–0.10 which is very close to that obtained for the longitudinal variance given in Fig. 12. The result for the pore shown in Fig. 2(d) is significantly below the others for all values of Re_{pore}. This consistent reduction of lateral variance is for the pore that has a strong longitudinal jet-like flow, with high shear rate conditions. The strong decrease in lateral variance is attributed to the strong mean jet-like flow which may inhibit lateral fluctuations. All data are seen to reach an asymptotic limit beyond Re_{pore} of 2860, similar to the longitudinal variance.

The ratio of the longitudinal to lateral velocity variance, v'/u', is a measure of local directional variations of the turbulence. Large differences can contribute to differences of the directional dispersion within the flow. This variance ratio was determined for each of the four pores and is shown in Fig. 14, for the highest Re_{pore} value, as contour plots within each of the four pores. The

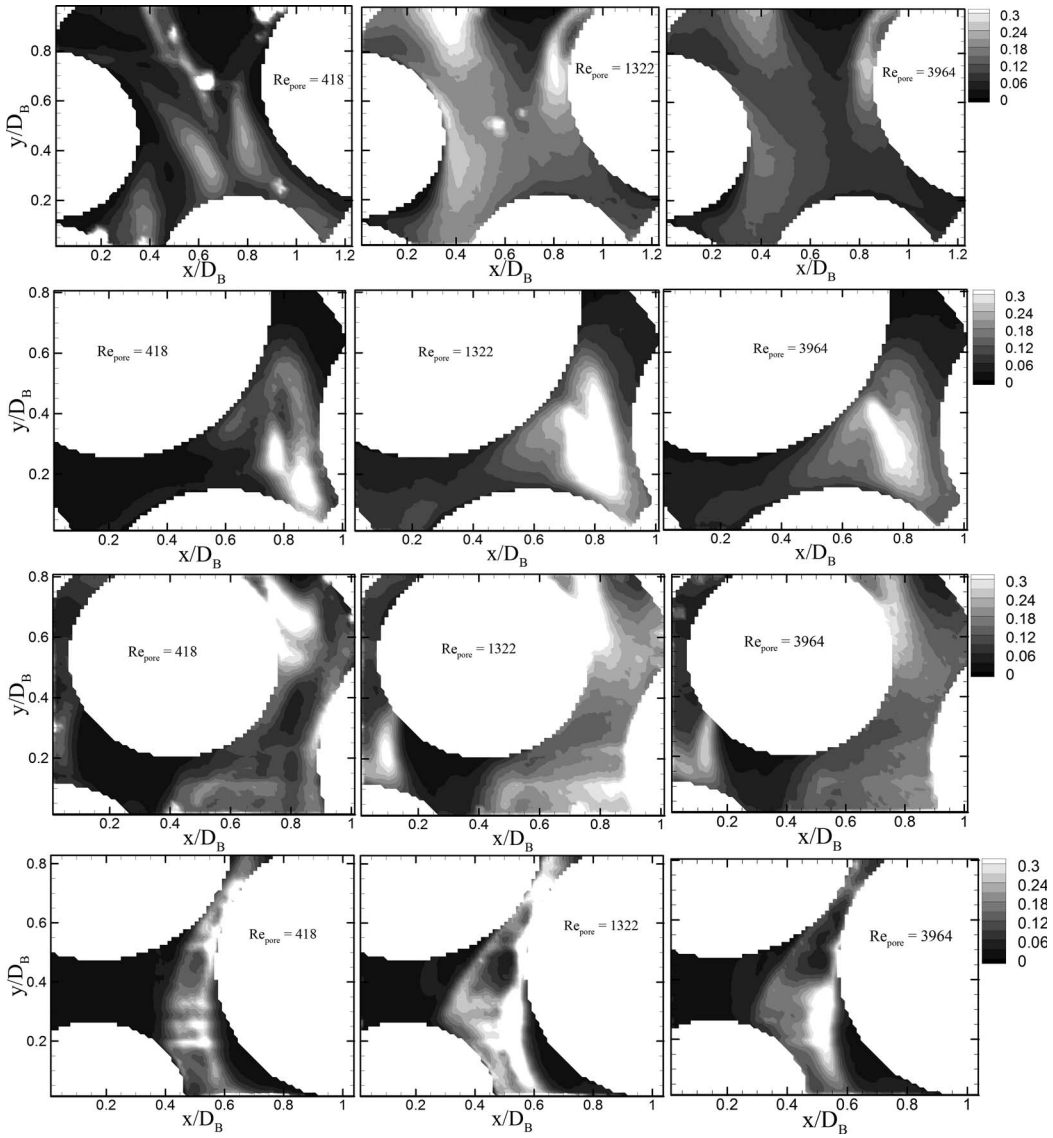

FIG. 10. Contour maps of normalized longitudinal fluctuating velocity variances, $v'^2/V_{int}{}^2$, for $Re_{pore} = 418$, $Re_{pore} = 1322$, Re_{pore} 2860, and $Re_{pore} = 3964$ for each of the pores shown in Fig. 2.

corresponding histograms are shown in Fig. 15. It is clear that flow geometry and the resultant mean flow structure influence the degree of variation between longitudinal and lateral variance. For the larger channel like flow of the pore shown in Fig. 2(a), there are essentially no differences between the two directional variances, with a much stronger peak of the histogram occurring at a ratio of 1. Whereas the other pore flows, which contain a larger degree of accelerated flow, jet-like behavior, or recirculation regions, have higher directional variations. For instance, the pore shown in Fig. 2(d) which has a jet-like flow structure shows very large values of the ratio of v'/u'. This indicates that the jetting condition reduces the lateral contribution to the fluctuating velocity component. In contrast to this, the large pore region of Fig. 2(a) results in the more homogeneous and isotropic type behavior with a very large peak of the histogram near 1.0.

In general, for these flows relatively high values of turbulence intensity are found to occur at high Re_{pore} values. This turbulent fluctuation, similar to other wall-bounded shear flows (Tennekes and Lumley[25]) can be expected to bring high momentum fluid closer to the solid boundaries which acts as a momentum sink. This action would increase the mean velocity gradients closer to the solid

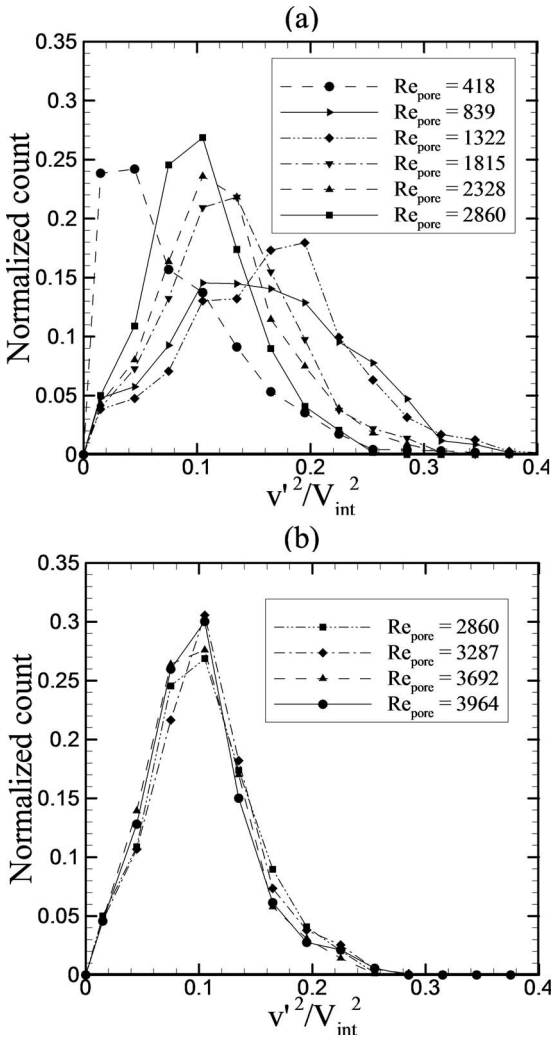

FIG. 11. Normalized longitudinal fluctuating velocity variance, $v'^2/V_{int}{}^2$, in the pore shown in Fig. 2(a) for (a) Re_{pore} = 418–2860 and (b) Re_{pore} = 2860–3964.

boundaries which would increase the bed pressure gradient for high Re_{pore} flows. To show how this contributes to the overall pressure drop along the flow in the bed, a simple scaling model is presented. To estimate the frictional pressure drop per length, $\Delta P_{fric}/L$, the contribution from the wall shear stress is written as

$$\frac{\Delta P_{fric}}{L} = \frac{\tau_w S}{\phi A L}, \tag{2}$$

where τ_w is shear stress at wall, S is total solid-liquid area, A is bed cross-sectional area, and L is bed length, consequently, the denominator on the right hand side represents the fluid volume. For a packing of uniform diameter spherical beads with diameter, D_B, the above equation becomes

$$\frac{\Delta P_{fric}}{L} = \frac{\tau_w(1-\phi)}{\phi}\frac{6}{D_B}. \tag{3}$$

To model the wall stress, we introduce the friction velocity, v_τ, based on $\tau_w = \rho v_\tau{}^2$ where ρ is the fluid density. Estimating the friction velocity, v_τ, to be proportional to the turbulent rms longitudinal velocity fluctuations, which was found to reach an asymptotic limit value of approximately $V_{int}/3$

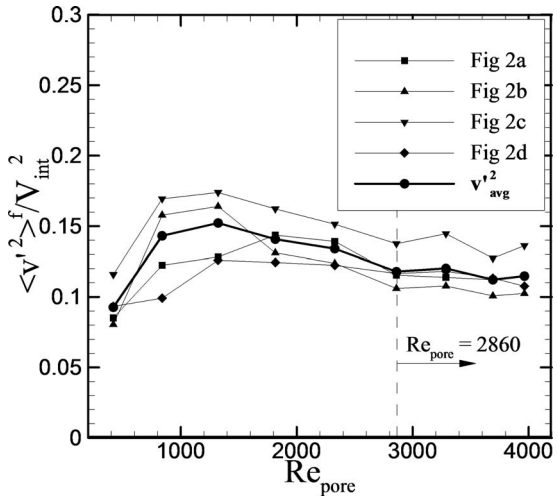

FIG. 12. Plot of normalized pore averaged fluctuating longitudinal velocity variances, $\langle v'^2\rangle^f / {V_{int}}^2$, versus Re_{pore} for the different pore geometries in Fig. 2.

(since $\boldsymbol{v'^2}_{\boldsymbol{avg}} \sim 0.11\ {V_{int}}^2$), results in

$$\frac{\Delta P_{fric}}{L} \approx \frac{2\rho(1-\phi)}{3\phi^3}\frac{V_{Darcy}^2}{D_B}, \tag{4}$$

where the average interstitial velocity, V_{int}, has been written in terms of the Darcy velocity, V_{Darcy} using the relationship $V_{int} = V_{Darcy}/\phi$. If we include the form drag, which is assumed to have a contribution estimated as proportional to the friction drag (say, as for creeping flow over a sphere), then

$$\frac{\Delta P}{L} \approx C\frac{\rho(1-\phi)}{\phi^3}\frac{V_{Darcy}^2}{D_B}, \tag{5}$$

where C is a constant which combines together the addition of the friction and form drag contributions which is expected to be $O(1)$ and the ratio of the fluctuating rms longitudinal velocity to interstitial velocity. For purpose of comparison, if the form drag to friction drag ratio is one, and using the

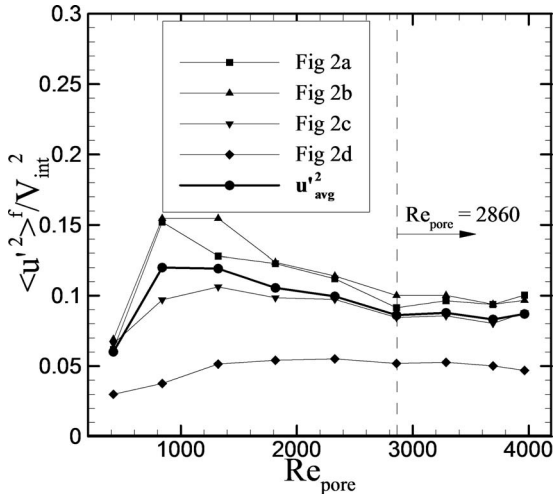

FIG. 13. Plot of the normalized pore averaged fluctuating transverse or lateral velocity variances, $\langle u'^2\rangle^f / {V_{int}}^2$, versus Re_{pore} for the different pore geometries in Fig. 2.

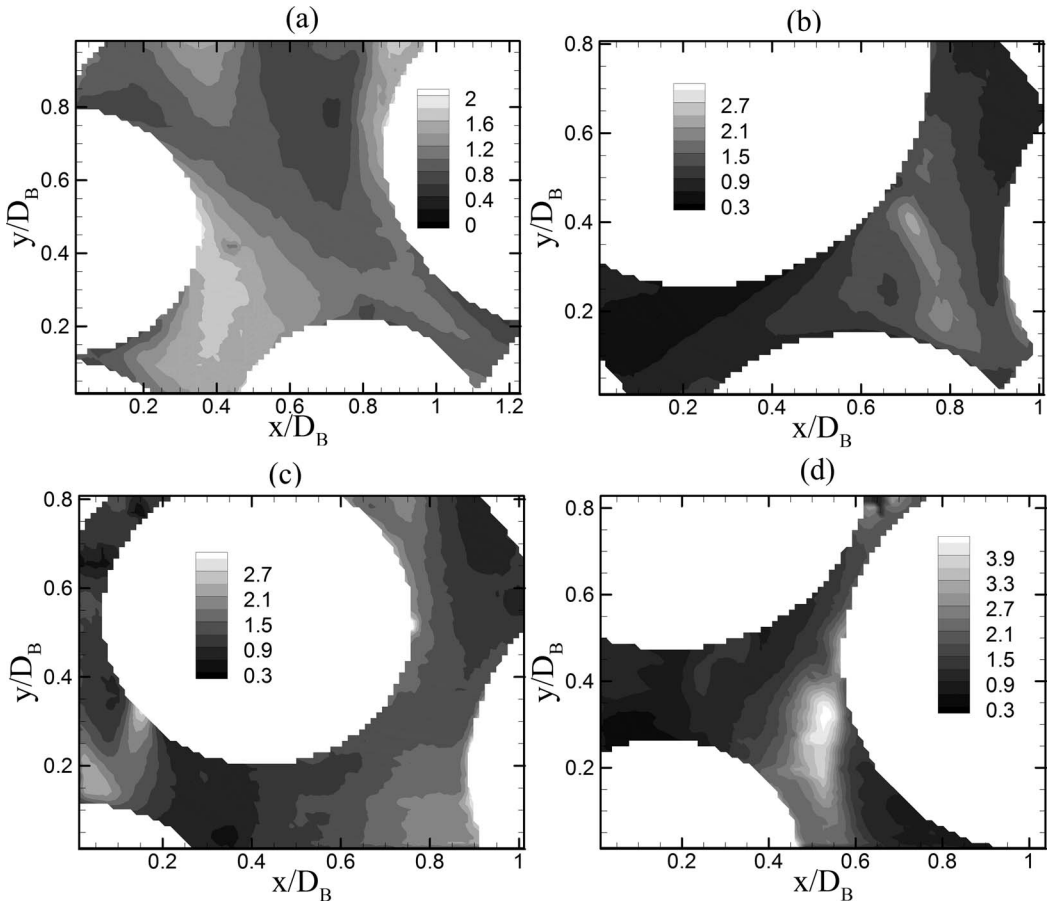

FIG. 14. (a)–(d) Ratio of longitudinal to lateral rms fluctuating velocity, v'/u', for $Re_{pore} = 3964$ for the four different pore geometries shown in Fig. 2.

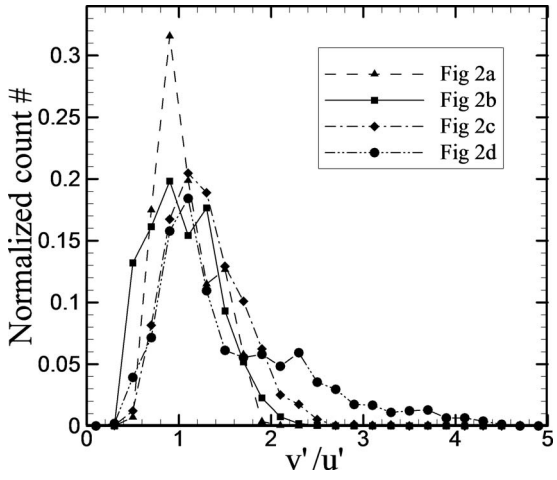

FIG. 15. Histogram of the ratio of longitudinal to lateral rms fluctuating velocity, v'/u', for $Re_{pore} = 3964$ for the four different pore geometries shown in Fig. 2.

measured value of 1/3 for the ratio of fluctuating rms velocity to interstitial velocity, then $C \sim 1.33$. The high Reynolds number contribution in the Ergun equation (Ergun[6]) is given as

$$\frac{\Delta P}{L} = 1.75 \frac{\rho(1-\phi)}{\phi^3} \frac{V_{Darcy}^2}{D_B}, \tag{6}$$

where the prefactor of 1.75 is on the order of the value of C above. Consequently, the fact that an asymptotic limit is reached for the fluctuating velocity variance anticipates that the pressure drop in the bed is consistent with the experimentally determined high Reynolds number limit for the bed pressure drop.

B. Dynamics of turbulence

An important measure of the turbulent kinetic energy dynamics has to do with the production term due to local mean shear. Similar to wall bounded flows like pipe flow, it can be expected that the high shear reasonably close to the walls, where Reynolds stress values remain high, produces significant portions of the turbulent kinetic energy for porous media flows. The viscous length scale, $\delta_\nu (=\nu/v_\tau)$, which serves as an indicator for the thickness of the viscous wall region, is estimated based on the above mentioned model for the frictional velocity to be approximately equal to the rms longitudinal velocity, which in turn is proportional to V_{int} in the large Reynold number limit. The result is

$$\delta_\nu = \frac{3}{\mathrm{Re}_{pore}} D_H. \tag{7}$$

For $Re_{pore} = 3964$ and $D_H = 12.45$ mm, used in the current study, the value of this viscous layer is 0.01 mm. This value is about an order of magnitude smaller than the vector resolution of 0.2 mm of this study, and consequently cannot be resolved.

However, in porous media flows, due to the complex geometry, there are many regions of high shear away from solid boundaries depending on the local mean flow conditions which can contribute to the overall production rate. The mean shear production, P_{12}, was evaluated based on its definition of the product of the turbulent cross correlation with the mean shear rates. The two-dimensional flow field data allow direct measurement of the pore averaged contributions given by $\langle P_{12} \rangle = -\overline{uv}(\partial U/\partial y + \partial V/\partial x)$. The results for each of the four pores versus Re_{pore} are given in Fig. 16 with the production rate scaled by the hydraulic diameter and interstitial velocity of the bed. The corresponding histograms of the scaled distributions of the production rate for the flow shown in Fig. 2(a) is given in Fig. 17 versus Re_{pore}. The histograms show asymmetric distributions centered around zero. As the Reynolds number increases, the distributions skew towards higher values of positive production, indicating regions of higher turbulent energy production at higher Re_{pore} values. In Fig. 16, it is shown that the scaled production rate reaches an apparent asymptotic limit beyond Re_{pore} of 2860 for all pore geometries. The asymptotic value of the area weighted averaged scaled production rate, $P_{12,avg}$, for all pores is approximately 0.07 $V_{int}{}^3/D_H$ with a range of 0.06–0.09.

C. Statistical description of mean velocity field

The variance of the mean longitudinal velocity relative to the local pore average value, $\langle (V - V_{int})^2 \rangle^f / V_{int}{}^2$ is shown in Fig. 18 versus Re_{pore} for all four pores shown in Fig. 2. This measure is important with regard to turbulent dispersion as it represents contribution to scalar spreading due to changes in sampled fluid velocity. The associated histogram for the flow shown in Fig. 2(a) for all values of Re_{pore} are shown in Fig. 19. In all cases, the mean longitudinal velocity variance decreases towards an asymptotic limit with increasing Re_{pore}. The asymptotic limit to reach a constant value seems to be at least 2860 for these data, although the pore in Fig. 2(a), the channel-like flow, is shown to be lower than the others and reaches its limit at a much lower value of Re_{pore}. The latter condition is further confirmed in the histogram showing a collapse of the distribution for Re_{pore} beyond approximately 1800. The reason for this particular pore reaching an asymptotic limit at a lower value of Re_{pore} than the others may be a consequence of the rather wide flow area,

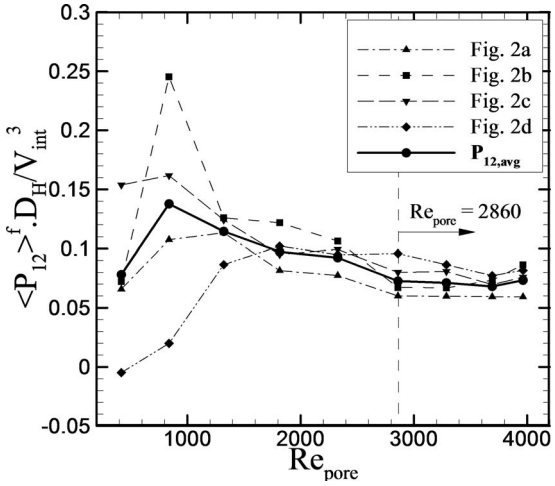

FIG. 16. Pore averaged turbulent kinetic energy production rate, $\langle P_{12}\rangle^f$, due to shear rate scaled by $V_{int}{}^3/D_H$, versus Re_{pore}, for the four pore spaces shown in Fig. 2.

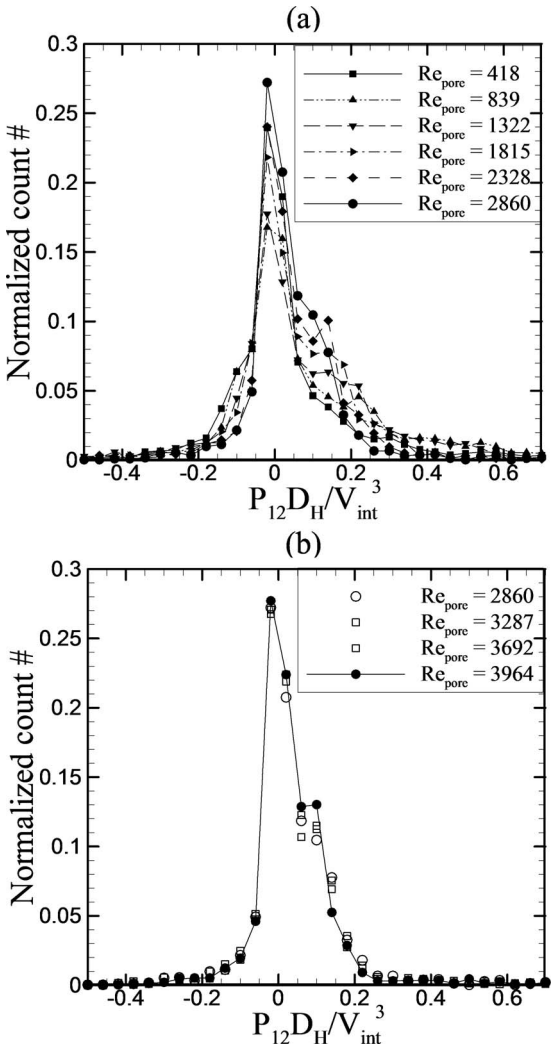

FIG. 17. Histogram of the normalized turbulent kinetic energy production, P_{12}, for the pore shown in Fig. 2(a) for (a) Re_{pore} = 418–2860 and (b) Re_{pore} = 2860–3964.

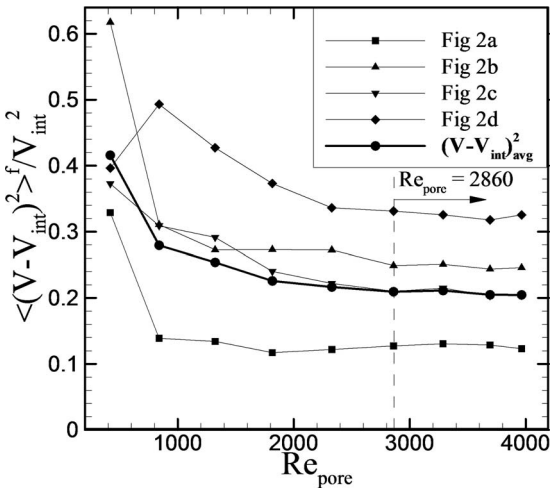

FIG. 18. Pore averaged mean Eulerian longitudinal velocity variance, $\langle (V - V_{int})^2 \rangle^f / {V_{int}}^2$, versus $\mathrm{Re}_{\mathrm{pore}}$ in the four pores shown in Fig. 2 versus Re_{pore}.

or large value of pore volume compared with the other flow geometries, which results in a more uniform mean flow through this pore. The average value for all pores is indicated in the figure as $(V - V_{int})^2_{avg}$ with an asymptotic value of 0.2 and a range of 0.12–0.34. The very large mean longitudinal velocity variance associated with the jet-like flow conditions of Fig. 2(d) corresponds with the results of Fig. 14 showing larger ratio of v′/u′. Consequently, these data indicate that the mean velocity variance shows a larger variation from pore-to-pore than the turbulence variance, most likely due to the formers stronger geometric dependence.

The results can be used to estimate the asymptotic dispersion characteristics based on local mean velocity measurements and the turbulence quantities. This is done by using the basic relationship (Tennekes and Lumley,[25] Taylor[27]) for the longitudinal dispersion coefficient, D_L, in terms of the Lagrangian time scale T_L and mean Lagrangian velocity variance of an ideal tracer, $\overline{v_L^2}$

$$D_L \cong \overline{v_L^2} T_L. \tag{8}$$

If it is assumed that the pore regions identified in this study constitutes all, or most, of the expected regions in a large randomly packed porous bed and hence are representative of what is experienced by a wandering ideal tracer as it samples different parts of the bed, then measured velocity variances and integral scales can be used to estimate the value of D_L. The Lagrangian velocity variance of an ideal tracer receives contribution from the mean Eulerian velocity variance, $\langle (V - V_{int})^2 \rangle^f$, and the fluctuating Eulerian velocity variance, $\langle v'^2 \rangle^f$

$$\overline{v_L^2} = \langle v'^2 \rangle^f + \langle (V - V_{\mathrm{int}})^2 \rangle^f. \tag{9}$$

Using the measured Eulerian mean square longitudinal velocity fluctuation of $\langle v'^2 \rangle^f \approx 0.11 {V_{\mathrm{int}}}^2$ and the range of measured values of the mean longitudinal velocity variance of $\langle (V - V_{\mathrm{int}})^2 \rangle^f \approx 0.12 {V_{\mathrm{int}}}^2 - 0.34 {V_{\mathrm{int}}}^2$, the longitudinal dispersion coefficient can be determined from an estimate of the Lagrangian time scale, T_L. Using the scaling argument as suggested by Tennekes and Lumley[25]

$$T_L \approx \alpha \frac{l_{pore}}{v'}, \tag{10}$$

where α is a constant of $O(1)$, l_{pore} is the integral mixing length scale and v' is the rms value of the fluctuating velocity. Using the asymptotic limits for these length and velocity scales, and $\alpha \sim 1$, then

$$T_L \approx \frac{D_H/5}{V_{\mathrm{int}}/3} \approx 0.6 \frac{D_H}{V_{\mathrm{int}}}. \tag{11}$$

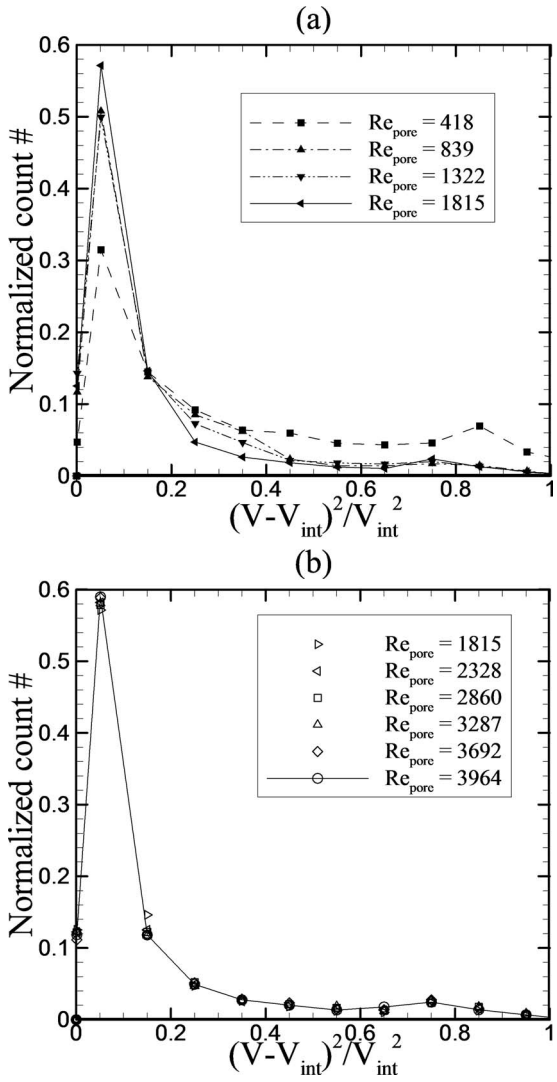

FIG. 19. Histograms of the mean Eulerian longitudinal velocity variance, $(V - V_{int})^2/V_{int}^2$, in the pores shown in Fig. 2(a) for (a) $Re_{pore} = 418$–1815 and (b) $Re_{pore} = 1815$–3964.

Combining these results and nondimensionalizing using the interstitial velocity, V_{int} and hydraulic diameter, D_H, the longitudinal dispersion coefficient becomes

$$\frac{D_L}{V_{\text{int}} D_H} \approx 0.14\text{–}0.27. \tag{12}$$

Since $D_B = 0.83 D_H$, then this can be written as $D_L \sim 0.12$–$0.22(V_{int} D_B)$. The above result represents the mechanical dispersion which should be valid for very high Peclet number flows in the absence of molecular diffusion effects. It has been proposed that the asymptotic limit for $D_L/(V_{int} D_B)$ for high Peclet numbers is 0.5 (Wen and Fan,[8] Delgado[28]). This has not been rigorously determined experimentally, although some global data based on concentration measurements suggest this limit (see Fig. 10 in Delgado[28]). Nevertheless, the dispersion coefficient estimated in Eq. (12) shows the correct dimensionality and the order of the constant compares well with the suggested limit. In fact, for $\alpha = 2.5$ (which is within the approximation limits suggested by Tennekes and Lumley[25]) and using an average of the range for the mean velocity variance in Fig. 18, the value of $D_L/(V_{int} D_B) = 0.5$. These results indicate that local time varying velocity data sets provide consistent results for longitudinal dispersion. However, this data set is small at this point and further analyses needs to be

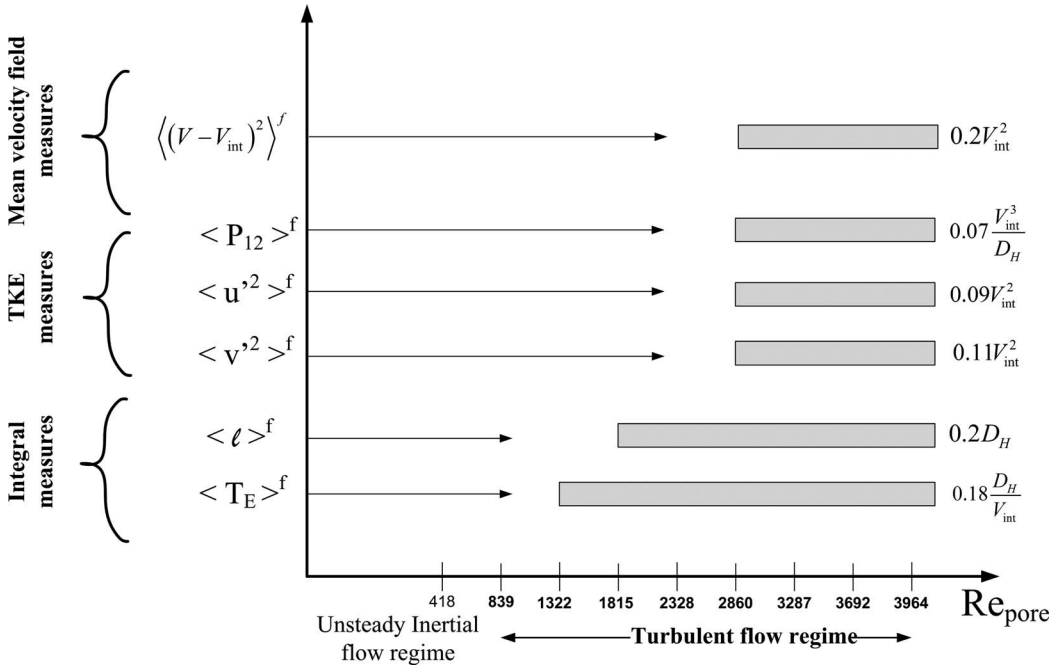

FIG. 20. Asymptotic limits for various measures of turbulent flow measured within the randomly packed porous bed.

carried out for a wide range of representative pores in a random packed bed to best determine this asymptotic limit.

D. Summary

The results presented of the various measures of turbulent quantities, in normalized form, are summarized in Fig. 20. The horizontal bars represent the range of Re_{pore} over which the asymptotic values were determined to be valid for these representative pores. Bed averaged variables (hydraulic diameter and average interstitial velocity) have been shown to scale the different flow turbulence measures reasonably well in that they tend to collapse data from all seemingly very disparate flow geometries. This trend shows that integral scales of turbulence in porous media flows are more strongly associated with global bed parameters like bead packing, bead diameter, porosity, and average interstitial velocity rather than properties associated with local mean flow structures. The integral scales of length and time are shown to reach their asymptotic limits near Re_{pore} between 1322 and 1815. Whereas the other turbulent statistical quantities require slightly higher values of Re_{pore}, closer to 2860. This possibly suggests that integral scales of turbulence responsible for interacting with mean velocity field asymptote before smaller scales of turbulence. The values of Re_{pore} used to identify these limits are based on the values used in the experiments and are not in any way expected to be exact, rather they provide a reasonable estimate of asymptotic limiting ranges. While all of these turbulence measures reach asymptotic values that are reasonably consistent from pore to pore, the variance of the mean velocity within the different pores shows a wider variation – which is indicative of the stronger association with the local bead arrangements. This then is shown to lead to a range of estimates of the dispersion coefficient.

V. CONCLUSIONS

Detailed measurements using time resolved PIV were obtained within a randomly packed porous bed using index matching over a range of pore Reynolds number of 418–3964. These data were analyzed to determine the turbulence characteristics within the flow. To do this, four selected pores

were identified which represented very different mean flow structures and used to show the Re_{pore} dependence on the scaled turbulence quantities. These results indicate that the statistical turbulence quantities scale well with the bed averaged parameters, namely, the hydraulic diameter, D_H, and the averaged interstitial velocity, V_{int}, for all of the pores evaluated. The only contrary result is the variance of the mean velocity within a pore, here it is found that the strong recirculation and jet-like regions that may occupy a pore dominate and strongly change the mean variance even when scaled by the average interstitial velocity. Measures of the turbulence quantities such as turbulent kinetic energy components and its shear production rate are shown to collapse towards asymptotic values for sufficiently high Re_{pore}, which here is shown to be approximately 2800. Whereas the integral Eulerian time scale and length scale are shown to reach asymptotic limits at lower values of Re_{pore}, less than 2000. Although these results are somewhat limited, as they are based on a few representative pores within the flow, they illustrate that a wide range of local flow geometries within a randomly packed porous bed exhibit scales of turbulent flow that are much smaller than the characteristic pore size and as such reach asymptotic limits seemingly independent of the pore geometry. Results have been used to obtain estimates of the mechanical dispersion coefficient based on the local time varying velocity measurements. Based on this it is shown that the limiting value for high Peclet number flows are consistent with those obtained using global measurements in very long test beds. More extensive data sets are recommended to evaluate results for a large number of pores in a relatively long test bed.

ACKNOWLEDGMENTS

This study was supported in part by NSF through grant 0933857 under the Particulate and Multiphase Processing Program, Dr. Ashok S. Sangani, Project Manager, and is gratefully acknowledged.

[1] M. J. S. De Lemos, *Turbulence in Porous Media: Modeling and Applications* (Elsevier, London, 2012).
[2] A. Dybbs and R. V. Edwards, "A new look at porous media fluid mechanics-Darcy to turbulent," *Fundamentals of Transport Phenomena in Porous Media* (Martinus Nijhoff, Dordrecht, 1984), Vol. 82, p. 201.
[3] P. Andrigo, R. Bagatin, and G. Pagani, "Fixed bed reactors," Catal. Today **52**, 197 (1999).
[4] G. Eigenberger, "Fixed-Bed Reactors," *Ullmann's Encyclopedia of Industrial Chemistry* (Wiley-VCH Verlag GmbH & Co. KGaA, 2000).
[5] A. Dixon and D. Cresswell, "Effective heat transfer parameters for transient packed-bed models," AIChE J. **32**, 809 (1986).
[6] S. Ergun, "Fluid flow through packed columns," Chem. Eng. Prog. **48**, 89 (1952).
[7] D. Gunn, "Axial and radial dispersion in fixed beds," Chem. Eng. Sci. **42**, 363 (1987).
[8] C. Y. Wen and L. Fan, *Models for Flow Systems and Chemical Reactors* (Dekker, New York, 1975).
[9] M. J. S. de Lemos and M. H. J. Pedras, "Recent mathematical models for turbulent flow in saturated rigid porous media," J. Fluids Eng. **123**, 935 (2001).
[10] B. V. Antohe and J. L. Lage, "A general two-equation macroscopic turbulence model for incompressible flow in porous media," Int. J. Heat Mass Transfer **40**, 3013 (1997).
[11] D. Getachew, W. J. Minkowycz, and J. L. Lage, "A modified form of the κ–ϵ model for turbulent flows of an incompressible fluid in porous media," Int. J. Heat Mass Transfer **43**, 2909 (2000).
[12] T. Masuoka and Y. Takatsu, "Turbulence model for flow through porous media," Int. J. Heat Mass Transfer **39**, 2803 (1996).
[13] A. Nakayama and F. Kuwahara, "A macroscopic turbulence model for flow in a porous medium," J. Fluids Eng. **121**, 427 (1999).
[14] M. H. J. Pedras and M. J. S. de Lemos, "Macroscopic turbulence modeling for incompressible flow through undeformable porous media," Int. J. Heat Mass Transfer **44**, 1081 (2001).
[15] M. A. Northrup, T. J. Kulp, S. M. Angel, and G. F. Pinder, "Direct measurement of interstitial velocity-field variations in a porous-medium using fluorescent-particle image velocimetry," Chem. Eng. Sci. **48**, 13 (1993).
[16] S. Saleh, J. F. Thovert, and P. M. Adler, "Measurement of two-dimensional velocity fields in porous media by particle image displacement velocimetry," Exp. Fluids **12**, 210 (1992).
[17] A. Y. L. Huang, M. Y. F. Huang, H. Capart, and R. H. Chen, "Optical measurements of pore geometry and fluid velocity in a bed of irregularly packed spheres," Exp. Fluids **45**, 309 (2008).
[18] A. Lachhab, Y. K. Zhang, and M. V. I. Muste, "Particle tracking experiments in match-index-refraction porous media," Ground Water **46**, 865 (2008).
[19] M. Moroni and J. H. Cushman, "Statistical mechanics with three-dimensional particle tracking velocimetry experiments in the study of anomalous dispersion. II. Experiments," Phys. Fluids **13**, 81 (2001).
[20] L. M. Peurrung, M. Rashidi, and T. J. Kulp, "Measurement of porous-medium velocity-fields and their volumetric averaging characteristics using particle tracking velocimetry," Chem. Eng. Sci. **50**, 2243 (1995).
[21] J. L. Stephenson and W. E. Stewart, "Optical measurements of porosity and fluid motion in packed-beds," Chem. Eng. Sci. **41**, 2161 (1986).

[22] V. A. Patil and J. A. Liburdy, "Flow characterization using PIV measurements in a low aspect ratio randomly packed porous bed," Exp. Fluids **54**, 1497 (2013).
[23] V. A. Patil and J. A. Liburdy, "Optical measurement uncertainties due to refractive index mismatch for flow in porous media," Exp. Fluids **53**, 1453 (2012).
[24] R. Adrian, K. Christensen, and Z. C. Liu, "Analysis and interpretation of instantaneous turbulent velocity fields," Exp. Fluids **29**, 275 (2000).
[25] H. Tennekes and J. L. Lumley, *A First Course in Turbulence* (The MIT Press, Cambridge, 1972).
[26] S. P. Burke and W. B. Plummer, "Gas flow through packed columns," Ind. Eng. Chem. **20**, 1196 (1928).
[27] G. Taylor, "Diffusion by continuous movements," Proc. London Math. Soc. **20**, 196 (1922).
[28] J. M. P. Q. Delgado, "A critical review of dispersion in packed beds," Heat Mass Transfer **42**, 279 (2006).